




Asphericity of magnetization density and anisotropy in rare-earth pyrochlores via polarized neutron diffraction and iterative entropy maximization

I. A. Kibalin  and A. Gukasov **Laboratoire Léon Brillouin, CEA-CNRS, CE-Saclay, 91191 Gif-sur-Yvette, France* (Received 21 July 2021; revised 28 January 2022; accepted 9 February 2022; published 11 March 2022)

The procedure of magnetization density reconstruction in locally anisotropic magnetics with unquenched orbital moment is developed, based on the iterative entropy maximization and the site susceptibility approach. The procedure provides simultaneously model-free site susceptibility parameters of the R ions and the shape of the magnetization distribution. The reconstruction of a noncollinear magnetic moment distribution was applied to rare-earth pyrochlore compounds $R_2\text{Ti}_2\text{O}_7$ ($R = \text{Tb}, \text{Ho}, \text{Er}, \text{Yb}$), which revealed an oblate asphericity of the Tb^{3+} magnetization density and a prolate one for the Ho^{3+} and Yb^{3+} ions. The noncollinear magnetic moment distributions are compared with these predicted by the single-ion anisotropy model, shedding light on the anisotropy of lanthanides with an unquenched orbital moment.

DOI: [10.1103/PhysRevB.105.104411](https://doi.org/10.1103/PhysRevB.105.104411)

I. INTRODUCTION

Lanthanide ions continue to play a crucial role in various research fields such as magnetic resonance imaging [1], single molecule-based storage devices [2–4], and multiferroics and spintronics [5]. Central to the development of all these fields is the local magnetic anisotropy that is due to the presence of orbital angular momentum in the ground state and a nonuniform distribution of electrons among the $4f$ orbitals subject to the electric field of a ligand environment. Since the magnetic anisotropy can be modified by appropriate combinations of ions and ligands, the information about the spatial distribution of spin, orbital, and electron densities in lanthanides can be used to rationalize an environment that will generate a ground state with desirable magnetic properties.

Information about the local magnetic anisotropy is currently obtained by electron paramagnetic resonance spectroscopy, providing the anisotropic g values of R ions [6], and angular-resolved or torque magnetometers [7]. These techniques, however, are not generally applicable for all space groups and site symmetries. For $4f$ elements the magnetic anisotropy can be estimated through crystal-field parameters obtained by using inelastic neutron scattering [8]. In contrast, a newly developed polarized neutron diffraction (PND) method presents a completely general approach to measuring both the anisotropic g values of an R ion and the orientation of its local anisotropy axes in the unit cell, regardless of crystal symmetry [9–12].

There is also much theoretical effort that aims at understanding and enhancing magnetic anisotropy in multiferroics and molecular magnetic materials [13]. Hence, the susceptibility parameters obtained by PND can be complemented by the information about the crystal-field ground state, which

can be obtained either from quantum-chemistry calculations or from optical and neutron spectroscopies [14].

Theoretical calculations show that the variation of magnetization anisotropy is accompanied by important changes in $4f$ -electron spin and orbital distributions. Note for $4f$ elements the determination of the crystal-field levels provides a single-ion ground state wave function that can be used to reconstruct the magnetization density. However, the reliability of such a reconstruction for low symmetry and hydrogen containing materials is yet to be demonstrated. Hence, there is a clear motivation to develop methods which could reveal these important features.

Recently, the asphericity of the $4f$ -electron (charge) distribution obtained by high-resolution x-ray diffraction has been used to determine the easy magnetic axis of the Dy^{3+} ion in Dy -molecular compounds [15]. We note, however, that the relation between the shapes of the electron and magnetization densities is rather complex. Therefore, more direct access to the shape of the magnetization distribution, including orbital and spin contributions, is required.

Polarized neutron diffraction (PND) is a well-established tool to investigate the spin density distribution in magnetic $3d$ compounds with a quenched orbital moment [16]. In this case by using the multipole model or maximum entropy methods (MEM) [17] one can get a detailed description of the spin density [18], or by employing the spin-resolved atomic orbital model, one can obtain the radial extension, orientation, and population of atomic orbitals of unpaired electrons [19]. However, the presence of an unquenched orbital magnetic moment in lanthanides leads to the appearance of noncollinearity in the magnetization distribution [20]. As a result, the magnetization distribution apart from the spin contribution contains an orbital one, which invalidates the conventional approaches to the spin density evaluation from PND.

Here, we show that combining the MEM reconstruction procedure with the local susceptibility approach [21], properly taking into account the local anisotropy, gives access

*arsen.goukassov@cea.fr

to the asphericity of the magnetization density. We illustrate the possibilities of the method by the joint magnetization density reconstruction and susceptibility refinement of locally anisotropic lanthanide pyrochlores $R_2\text{Ti}_2\text{O}_7$ ($R = \text{Tb}, \text{Ho}, \text{Er}$ and Yb).

II. POLARIZED NEUTRON DIFFRACTION

A. Local susceptibility approach

A PND experiment consists of using the Bragg diffraction of a monochromatic polarized neutron beam on a single crystal in a magnetic field (\mathbf{H}) and measuring the peak intensities with the neutron spin parallel and antiparallel to the field. The quantity measure in the PND experiment is the intensity asymmetry $A = (I^+ - I^-)/(I^+ + I^-)$. In this equation I^+ and I^- are the intensities of neutrons scattered with the incident polarization parallel (+) and antiparallel (−) to the applied magnetic field \mathbf{H} . At the field parallel to the vertical axis and perpendicular to the incident beam, the cross sections for Bragg scattering \mathbf{h} are [22]

$$I^\pm \sim F_N^2 + \mathbf{F}_{\mathbf{M}\perp}^2 \pm 2 \text{Re}[F_N(\mathbf{F}_{\mathbf{M}\perp}^* \cdot \mathbf{P})] \quad (1)$$

giving

$$A_{\mathbf{h}} = \frac{2 \text{Re}[F_N(\mathbf{F}_{\mathbf{M}\perp}^* \cdot \mathbf{P})]}{F_N^2 + \mathbf{F}_{\mathbf{M}\perp}^2}, \quad (2)$$

where F_N is the nuclear structure factor, $\mathbf{F}_{\mathbf{M}\perp}$ is the projection of the magnetic structure factor $\mathbf{F}_{\mathbf{M}}$ perpendicular to the scattering vector \mathbf{k} , and \mathbf{P} is the neutron polarization vector parallel to \mathbf{H} . If the magnetization within the unit cell can be assigned to independent atoms, so that each has a total moment, their response to an applied magnetic field \mathbf{H} can be described by the susceptibility tensor $\hat{\chi}_a$. Then the structure factor $\mathbf{F}_{\mathbf{M}}$ can be written as [21]

$$\mathbf{F}_{\mathbf{M}} = \sum_{a,s} f_a(\mathbf{k}) \hat{R}_s \hat{\chi}_a \hat{R}_s^{-1} \mathbf{H} \cdot e^{i\mathbf{k} \cdot (\hat{R}_s \mathbf{r}_a + \mathbf{t}_s)}. \quad (3)$$

\hat{R}_s and \mathbf{t}_s are the rotations and translations associated with the s th element of the space group and \mathbf{r}_a is the position of the atom a ; $f_a(\mathbf{k})$ is the magnetic form factor of the atom a .

Expressions (2) and (3) are currently used to refine the susceptibility tensor $\hat{\chi}_a$ assuming a spherical distribution of unpaired electrons and using the theoretical description of the magnetic form factor f_a [21]. Here, we show how they can be adapted to handle the asphericity and noncollinearity of the magnetization density in the reconstruction by the maximum entropy method (MEM).

B. MEM algorithm

Originally designed to reconstruct the most probable image in the situation of incomplete and/or noisy information, MEM is widely used in crystallography (for a review, see Refs. [23,24]). Maximum entropy produces strictly positive images, whereas the magnetization density can either be positive or negative. The approach, first used in NMR data analysis [25,26], is then to retrieve two positive densities ρ_i^+ and ρ_i^- , the difference of which is the desired magnetization density [17]. The first density ρ_i^+ represents the moments

along the applied field \mathbf{H} , while the second one ρ_i^- the moments opposite to the field direction. We extend this concept of two-channel entropy by adding a density ρ_i^x taking into account the local anisotropy of magnetic sites, which is responsible for the induced magnetization noncollinear with the applied field. Thus, the entropy S is defined as the sum of entropies of three positive magnetic densities,

$$S = - \sum_i \left(\rho_i^x \log \frac{\rho_i^x}{\rho_i^{x,p}} + \rho_i^+ \log \frac{\rho_i^+}{\rho_i^{+,p}} + \rho_i^- \log \frac{\rho_i^-}{\rho_i^{-,p}} \right) \quad (4)$$

where the sum over i runs through the unit cell discretized into a sufficiently fine grid. The prior densities $\rho_i^{x,p}$, $\rho_i^{\pm,p}$ can be taken as a constant function (so-called flat prior), or alternatively, as a nonuniform prior involving a spherical magnetic density distribution around magnetic atoms (for details, see the Supplemental Material [27]). In the absence of a noncollinear term ρ_i^x , expression (4) is reduced to the classical Papoular approach [17].

Introducing the noncollinear term all over the unit cell might strongly increase the calculation time and inhibit the convergence of the reconstruction. Therefore, the unit cell is partitioned into atomic basins. The density ρ_i^x is assigned to the basins of magnetic atoms to describe their anisotropic behavior, and the collinear densities ρ_i^\pm elsewhere in the unit cell. Such a simple space separation reduces the calculation time and the cross-correlation between these densities. It can be justified by the fact that the basin of magnetically anisotropic atoms can be predicted in advance.

The entropy S has a maximal value for densities ρ_i^x , ρ_i^\pm calculated iteratively according to the procedure proposed by Collins [28],

$$\rho_i^{(n+1)} = \rho_i^{(n)} \exp \left[-v \frac{\delta C}{\delta \rho_i} \right], \quad (5)$$

where $\rho_i^{(n+1)}$ is the new value, and $\rho_i^{(n)}$ is the value of the cycle before. The iterations start with the prior densities as the zeroth-order approximation to the magnetization density distribution $\rho_i^{(0)} = \rho_i^p$ with a subsequent renormalization after each cycle. The parameter v affects the convergence rate of the iterative procedure.

The measured data are included in the reconstruction procedure via a χ^2 -like sum $C = \frac{1}{N_{\mathbf{h}}} \sum_{\mathbf{h}} |A_{\mathbf{h}} - A_{\mathbf{h}}^{\text{exp}}|^2 / \sigma_{\mathbf{h}}^2$, with the observed values of the asymmetry parameters $A_{\mathbf{h}}^{\text{exp}}$, the number of observations is $N_{\mathbf{h}}$, and the estimated error of observations is $\sigma_{\mathbf{h}}$. The model asymmetry parameters $A_{\mathbf{h}}$ are related to magnetization density through the magnetic structure factor [Eq. (2)]. Replacing the magnetic form factor f_a in Eq. (3) by the Fourier transform of the magnetization density [29] gives

$$\mathbf{F}_{\mathbf{M}} = \frac{V}{N_p N_s} \sum_{i,s} [\rho_i^x \hat{R}_s \hat{\chi}_i^r \hat{R}_s^{-1} \mathbf{e}_{\mathbf{H}} + (\rho_i^+ - \rho_i^-) \mathbf{e}_{\mathbf{H}}] \times \exp[i\mathbf{k} \cdot (\hat{R}_s \mathbf{r}_i + \mathbf{t}_s)], \quad (6)$$

where the sum over i runs through all pixels in the unit cell; the sum over s includes all symmetry elements, N_s is the number of symmetry elements, and N_p is the number of pixels in the unit cell of volume V . The unitary susceptibility tensor $\hat{\chi}_i^r$ takes the values of $\hat{\chi}_a$ for the magnetic basins of ion a

normalized to the susceptibility along its easy magnetization axis. Hence, $\hat{\chi}_i^r$ reproduces the shape of the magnetic ellipsoid $\hat{\chi}_a$ but not its magnitude. $\hat{\chi}_i^r$ is equal to zero in the basin of nonmagnetic atoms and \mathbf{e}_H gives the direction of applied field \mathbf{H} . Note that in the susceptibility approach the distribution of magnetic moments within the basin of magnetic atoms is collinear and defined by the parameter $\hat{\chi}_i^r$.

The reconstructed densities ρ_i^x, ρ_i^\pm can be used for the refinement of susceptibility parameters by the minimization of a χ^2 -like sum C . In this way, MEM calculations and susceptibility refinement are alternately repeated until no changes occur in the susceptibility parameters. Thus, the proposed approach, apart from the magnetization density reconstruction, yields the susceptibility tensor $\hat{\chi}_a$.

Combining the densities and the local susceptibility parameters obtained by the MEM procedure, one can assess the distribution of the total magnetic moment in the unit cell induced in the magnetic field \mathbf{H} by using the expression

$$\mathbf{m}_i = [\rho_i^x \hat{\chi}_i^r \mathbf{e}_H + (\rho_i^+ - \rho_i^-) \mathbf{e}_H]. \quad (7)$$

As clearly seen from expression (7), ρ^x represents the magnetization density around the magnetic atoms, while the direction and magnitude of induced moments are determined by the unitary susceptibility tensor $\hat{\chi}^r$ and the applied field \mathbf{H}

III. MAGNETIZATION DENSITY IN RARE-EARTH PYROCHLORES

The MEM procedure described above was used for the density reconstruction in $R_2\text{Ti}_2\text{O}_7$ ($R = \text{Tb}, \text{Ho}, \text{Er}, \text{Yb}$) belonging to a large family of rare-earth pyrochlores. The pyrochlore lattice is a model for the geometrical magnetic frustration arising from the subtle interplay of single-ion anisotropy, exchange, and dipolar interactions [30,31]. Depending on the balance between these terms, one may observe spin-ice or spin-liquid behaviors, or complex magnetic orders stabilized by first-order transitions.

Pyrochlore orders in cubic symmetry and R ions are located on the $16d$ site of the space group $Fd\bar{3}m$. The principal axes of the magnetization ellipsoid are oriented along the four local $\langle 111 \rangle$ axes. The principal lengths of the ellipsoid along the local axes χ_{\parallel} and in perpendicular directions χ_{\perp} have been determined for each compound from the PND experiment performed earlier at the ORPHEE reactor of the Léon Brillouin Laboratory [9]. Flipping ratios were measured on the 6T2 diffractometer using neutrons of incident wavelength 1.4 \AA with polarization $P = 0.98$. We revisited the flipping ratio data sets measured at 5 K in the magnetic field of 1 T (applied in the $[110]$ direction), where the cooperative effects are still small for all compounds. The refinement and MEM reconstruction were made using the crystallographic library CRYSPY [32].

First, a conventional local susceptibility (LS) model refinement of data sets was performed using theoretical form factors of rare-earth ions, assuming spherical magnetic density distribution. The results of the refinements given in Table I were found in perfect agreement with these published earlier [9], confirming the strong Ising local anisotropy of Tb^{3+} and Ho^{3+} ions ($\chi_{\parallel} \gg \chi_{\perp}$) and the weak XY anisotropies of Er^{3+} and Yb^{3+} ions ($\chi_{\parallel} < \chi_{\perp}$).

TABLE I. Principal axes of magnetization ellipsoid $\chi_{\parallel}, \chi_{\perp}$ and goodness of fit (GOF) obtained by LS model refinement, the MEM procedure including susceptibility refinement (MEM), and calculations using the single-ion (SI) model.

	$\chi_{\parallel} (\frac{\mu_B}{T})$	$\chi_{\perp} (\frac{\mu_B}{T})$	GOF
$\text{Tb}_2\text{Ti}_2\text{O}_7$	$N_h = 199, \sin \theta_h / \lambda \leq 0.546 \text{ \AA}^{-1}$		
LS model	2.75(2)	0.23(2)	15.19
MEM	2.65(3)	0.20(3)	10.21
SI model	3.82	1.08	
$\text{Ho}_2\text{Ti}_2\text{O}_7$	$N_h = 228, \sin \theta_h / \lambda \leq 0.962 \text{ \AA}^{-1}$		
LS model	10.82(2)	0.02(2)	16.12
MEM	11.26(6)	0.04(6)	11.63
SI model	8.38	0.02	
$\text{Er}_2\text{Ti}_2\text{O}_7$	$N_h = 149, \sin \theta_h / \lambda \leq 0.766 \text{ \AA}^{-1}$		
LS model	0.59(1)	0.97(1)	4.53
MEM	0.60(1)	1.06(1)	2.02
SI model	0.60	1.72	
$\text{Yb}_2\text{Ti}_2\text{O}_7$	$N_h = 51, \sin \theta_h / \lambda \leq 0.454 \text{ \AA}^{-1}$		
LS model	0.36(6)	0.56(5)	2.14
MEM	0.44(3)	0.59(2)	1.85
SI model	0.12	0.59	

Then, the same sets of reflections were used for the MEM reconstruction of the magnetization density using the procedure above implemented recently in the CRYSPY library [32]. The density distribution was discretized into $144 \times 144 \times 144$ pixels along the a, b , and c axes and a spherical prior density ρ_i^x , calculated by using Slater-type radial functions for rare-earth ions [33], was used in the reconstruction (a possibility of using a uniform prior is also discussed in the Supplemental Material [27]). The unit cell was partitioned into magnetic basins, defined as the regions of space closest to a given magnetic atom using Voronoi diagrams [34]. Basins resulting from the partition have the shape of polyhedra with their orientation being defined by crystal symmetry (see Fig. 1). Details of the partition are given in the Supplemental Material [27]. The parameters of MEM reconstruction are

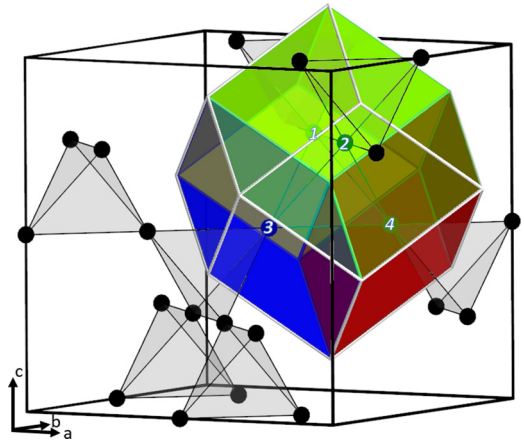


FIG. 1. The magnetic basins of four rare-earth ions belonging to one tetrahedron are shown by yellow (1), green (2), blue (3), and red (4) polyhedra. Black tetrahedra represent a rare-earth sublattice of the pyrochlore structure.

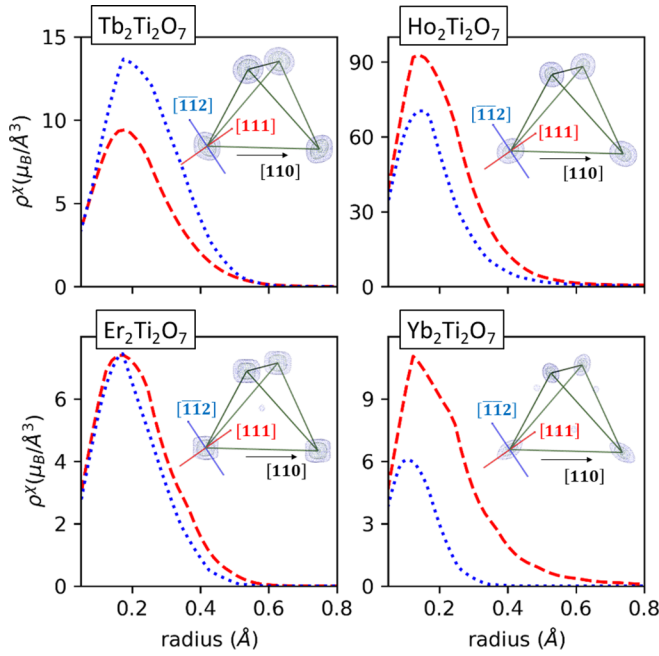


FIG. 2. The magnetization density of rare earth along the $[111]$ axis (red dashed lines) and along $[10\bar{1}]$ axis (blue dotted lines) for $\text{Tb}_2\text{Ti}_2\text{O}_7$, $\text{Ho}_2\text{Ti}_2\text{O}_7$, $\text{Er}_2\text{Ti}_2\text{O}_7$, and $\text{Yb}_2\text{Ti}_2\text{O}_7$ at 5 K in 1 T after MEM reconstruction. The density isosurfaces of four R ions are shown in the insets.

given in Table I in comparison with the single-ion (SI) model calculations. As expected, a better goodness of fit due to the more adjustable parameters is seen.

One can see that MEM calculations give better data descriptions and confirm the Ising character of Ho^{3+} and Tb^{3+} ions and the XY one of Er^{3+} and Yb^{3+} . Surprisingly, the susceptibility parameters obtained by the LS model and MEM are found to be very close. The agreement between these approaches indicates that the LS model gives reliable susceptibility parameters in spite of using a spherical approximation of the magnetic form factor. Taking into account of the asphericity of the magnetization density by MEM improves the goodness of fit but shows very little influence on the susceptibility parameters.

The densities ρ_i^x reconstructed by MEM are shown as insets in Fig. 2. They represent the distribution of the modulus of magnetic moments induced by the field applied along the local easy magnetization axis of the ion. One can see that the density shapes of all compounds are close to spherical with either oblate (equatorially extended) or prolate (axially extended) distortion (we note that the reconstructions does not reveal any significant density outside the rare-earth basins). The asphericities of Ho^{3+} , Tb^{3+} , and Yb^{3+} are well pronounced, while that of Er^{3+} has a kind of cubic shape. This can be seen from Fig. 2 where the radial distributions of magnetization density parallel and perpendicular to the local anisotropy axis ($[111]$ and $[\bar{1}\bar{1}2]$) are shown. We found that the radial distributions reconstructed by the MEM procedure reproduce rather well the theoretical radial distribution of $4f$ ions. We note as well that the shape of magnetization densities is not correlated with the shape of magnetization ellipsoids.

Among Ising-type compounds, the canonical spin-ice $\text{Ho}_2\text{Ti}_2\text{O}_7$ compound yields slightly prolate magnetization density, with elongation axes oriented toward the center of the tetrahedron, while the spin-liquid one, $\text{Tb}_2\text{Ti}_2\text{O}_7$, shows an oblate magnetization distribution, compressed in the same direction.

The prolate shape of magnetization density in $\text{Ho}_2\text{Ti}_2\text{O}_7$ is in agreement with the saturated state $|M_J = \pm J\rangle$ of Ho^{3+} (where M_J is the angular momentum projection quantum number), as the oblate electron (charge) density of the free ion minimizes its crystal-field energy when the moment is oriented in the negative charge dense direction [35]. The saturated state $|M_J = \pm J\rangle$ of Ho^{3+} is also in accordance with bulk magnetization and neutron scattering results. In contrast, the spin-liquid $\text{Tb}_2\text{Ti}_2\text{O}_7$ shows an oblate magnetization distribution and rather weak magnetic moment of Tb^{3+} ion $2.17\mu_B$ induced at 5 K in 1 T (see Table I). Both features are incompatible with the saturated state $|M_J = \pm J\rangle$ of Tb^{3+} ($9.7\mu_B$), so we suggest that the oblate shape of the magnetization density in this case is due to the fact that the ground state of Tb^{3+} is far from the high moment $M_J = 6$ state. The soft Ising character of its local anisotropy and low magnetic moments observed in the field ordered magnetic states [36,37] corroborates this suggestion.

As far as XY-type compounds are concerned, it is seen that the density shape in $\text{Er}_2\text{Ti}_2\text{O}_7$ deviates from the spherical and this in $\text{Yb}_2\text{Ti}_2\text{O}_7$ has a prolate distortion (see Fig. 2). We note that theoretical predictions for the magnetization density shape for $\text{Er}_2\text{Ti}_2\text{O}_7$ are rather uncertain, as it shows a long-range magnetic order at 1.2 K. As a result, the ground state of the Er ions might be governed by an exchange molecular field, rather than by an external one. This is supported by the fact that the SI model overestimates the induced magnetic moments for this compound (see Table I).

We have reconstructed noncollinear magnetic moment distributions \mathbf{m}_i corresponding to our experimental conditions, i.e., field of 1 T applied in the $[110]$ direction at 5 K. Figure 3 displays the section of the distribution around the R ion in position $(0.5, 0.5, 0.5)$ in the plane $[110]$ - $[001]$. To visualize the noncollinearity we use the color wheel, where the red color corresponds to the collinear moment, and yellow and purple ones to those deviated from the field in the clockwise and anticlockwise directions, respectively. As seen from Fig. 3, the application of magnetic field in the $[110]$ direction induces noncollinear magnetic moment distributions in all compounds. Ising-type compounds yield the purple color, which corresponds to the deviation of the moments in the anticlockwise rotation from the field direction to the local easy magnetic $[111]$ axis. XY-type compounds show the moments closer to the field direction and slightly deviated in the opposite direction. The resulting integrated moments of the ions are also shown in the figure.

In order to compare these results with theory, we have calculated the magnetic moment distribution for different R ions in the same position in a magnetic field of 1 T at 5 K by using the SI anisotropy model. Calculations were made using the MCPHASE software suit [38] with the crystal-field (CF) parameters from Malkin *et al.* [39] and the simulated distributions of magnetic moments are shown in Fig. 4.

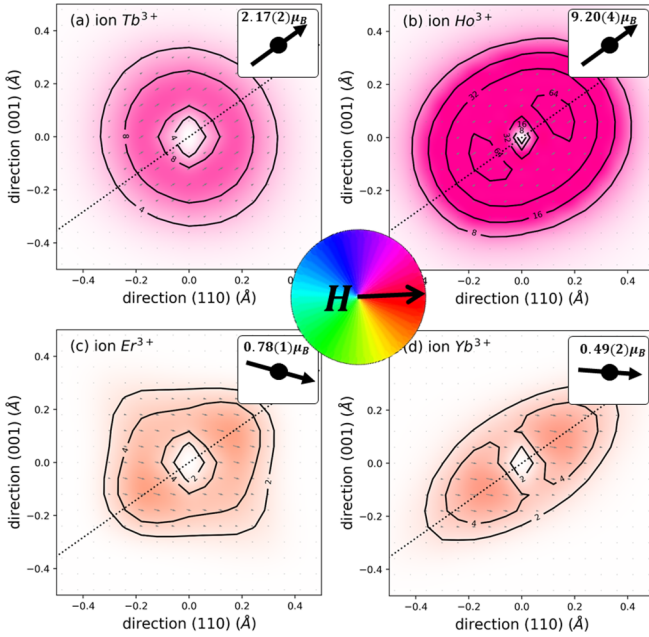


FIG. 3. The sections of magnetic moment distributions around the R ion in position $(0.5, 0.5, 0.5)$ in the plane $[110]$ - $[001]$. The distributions are reconstructed for a field of 1 T applied in the $[110]$ direction at 5 K by the MEM procedure. The crystallographic direction $[111]$ is shown by the dotted line. Arrows and colors show the orientation of induced magnetic moments. The color wheel is used to visualize the noncollinear regions of magnetization. Red color is used for collinear moments, and yellow and purple ones for clockwise and anticlockwise moment deviations from the field. The modulus of magnetic moments is shown by isodensities in units $[\mu_B/\text{\AA}^3]$. Orientations and values of integrated atomic moments of the ions are shown in the insets.

We should note that the comparison of our results with calculations is not straightforward, first, because MEM reconstruction reproduces the magnetization density, i.e., only a projection of the local magnetization distribution on one particular direction. This results in the collinear orientation of magnetic moments in magnetic basins, hence producing the monochrome MEM maps (Fig. 3). MCPHASE simulations, in turn, produce the magnetization distributions as a vector field and due to the spin-orbit interaction this leads to the appearance of noncollinearity within the ions manifesting itself in multicolor maps (Fig. 4). Second, the resolution of our PND measurements was not sufficiently high to see the fine details of the inner part of the magnetization density. Therefore, we shall limit our comparison to the most general features of experimental and theoretical densities.

As seen from the figure, the shapes of magnetic distributions for Tb^{3+} , Er^{3+} , and Yb^{3+} ions are in qualitative agreement with MEM results. In contrast, the simulations for Ho^{3+} ion yield an oblate shape of the distribution, while our results leans in favor of weak prolate asphericity. In the meantime, the rather low magnetic moment of Ho^{3+} ($6.85\mu_B$) obtained in the simulation seems to be incompatible with the saturated state $|M_J = \pm J|$. We suggest that this is because of the fact that the CF parameters in Ref. [39] were determined by using mean-field self-consistent calculations and an

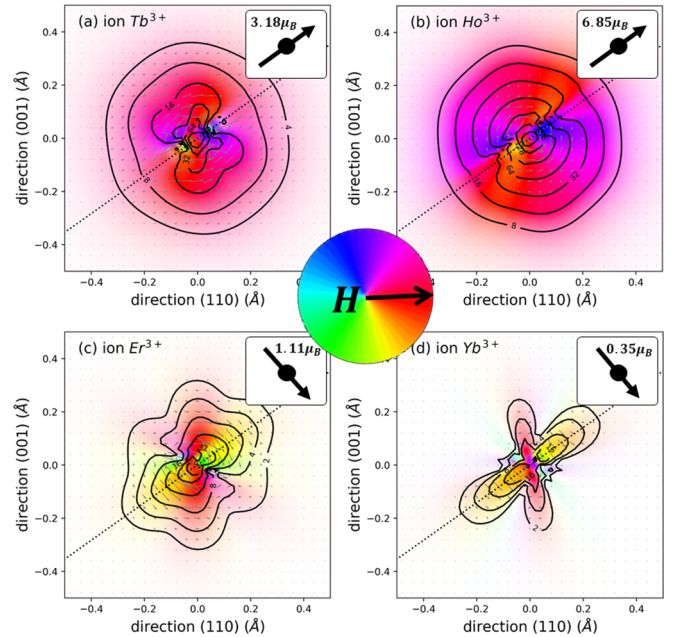


FIG. 4. The sections of magnetic moment distributions around the R ion in position $(0.5, 0.5, 0.5)$ in the plane $[110]$ - $[001]$. The distributions are calculated for a field of 1 T applied in the $[110]$ direction at 5 K using the SI model. The notation is the same as in Fig. 3.

anisotropic two-ion exchange tensor, which were not included in our simulations.

IV. CONCLUSION

A method of joint magnetization density MEM reconstruction and susceptibility refinement from PND data has been developed and successfully applied to lanthanide pyrochlores. Asphericity of the magnetization density in pyrochlores is observed and field-induced magnetic moment distributions are revealed. While the current approach is based on the constraints of collinearity of the moment distribution within the atomic basins, a lifting of this constraint can be envisaged once more extended PND data sets will be available on the new generation neutron spallation sources under construction [40].

The asphericities observed in $\text{R}_2\text{Ti}_2\text{O}_7$ should stimulate the development of direct methods of noncollinear magnetization density reconstruction in locally anisotropic compounds based on the joint multipole- or wave-function refinements [41], which should shed light on the anisotropy of compounds with unquenched orbital moments, primarily of lanthanides and iridates.

ACKNOWLEDGMENTS

We would like to thank X. Fabreges, I. Mirebeau, and J. Overgaard for a long-term collaboration and stimulating discussions. This work has been partially supported by the European Union's Horizon 2020 research and innovation program under Grant Agreement No. 871072. I.K. thanks CEA for his postdoctoral position.

- [1] M. Bottrill, L. Kwok, and N. Long, *Chem. Soc. Rev.* **35**, 557 (2006).
- [2] M. Leuenberger and D. Loss, *Nature (London)* **410**, 789 (2001).
- [3] F. Troiani and M. Affronte, *Chem. Soc. Rev.* **40**, 3119 (2011).
- [4] C. Godfrin, A. Ferhat, R. Ballou, S. Klyatskaya, M. Ruben, W. Wernsdorfer, and F. Balestro, *Phys. Rev. Lett.* **119**, 187702 (2017).
- [5] S. Sanvito, *Chem. Soc. Rev.* **40**, 3336 (2011).
- [6] F. Liu, D. Krylov, L. Spree, S. Avdoshenko, N. Samoylova, M. Rosenkranz, A. Kostanyan, T. Greber, A. Wolter, B. Büchner, and A. Popov, *Nat. Commun.* **8**, 16098 (2017).
- [7] M. Perfetti, G. Cucinotta, M.-E. Boulon, F. El Hallak, S. Gao, and R. Sessoli, *Chem. Eur. J.* **20**, 14051 (2014).
- [8] B. Paci, R. Caciuffo, G. Amoretti, O. Moze, K. H. J. Buschow, and A. P. Murani, *Solid State Commun.* **94**, 489 (1995).
- [9] H. Cao, A. Gukasov, I. Mirebeau, P. Bonville, C. Decorse, and G. Dhalenne, *Phys. Rev. Lett.* **103**, 056402 (2009).
- [10] E. Klahn, C. Gao, B. Gillon, A. Gukasov, X. Fabrèges, R. Piltz, S.-D. Jiang, and J. Overgaard, *Chem. Eur. J.* **24**, 16576 (2018).
- [11] K. Ridier, B. Gillon, A. Gukasov, G. Chaboussant, A. Cousson, D. Luneau, A. Borta, J.-F. Jacquot, R. Checa, Y. Chiba, H. Sakiyama, and M. Mikuriya, *Chem. Eur. J.* **22**, 724 (2016).
- [12] K. Ridier, A. Mondal, C. Boilleau, O. Cador, B. Gillon, G. Chaboussant, B. Le Guennic, K. Costuas, and R. Lescoužec, *Angew. Chem., Int. Ed.* **55**, 3963 (2016).
- [13] F. Gendron, B. Pritchard, H. Bolvin, and J. Autschbach, *Dalton Trans.* **44**, 19886 (2015).
- [14] A. Scheie, V. O. Garlea, L. D. Sanjeeva, J. Xing, and A. S. Sefat, *Phys. Rev. B* **101**, 144432 (2020).
- [15] C. Gao, A. Genoni, S. Gao, S. Jiang, A. Soncini, and J. Overgaard, *Nat. Chem.* **12**, 213 (2020).
- [16] P. Becker and B. Gillon, in *Modern Charge-Density Analysis* (Springer, Dordrecht, 2012), pp. 277–302.
- [17] R. Papoular and B. Gillon, *Europhys. Lett.* **13**, 429 (1990).
- [18] F. Givord, J.-X. Boucherle, P. Burlet, B. Gillon, and S. Kunii, *J. Phys.: Condens. Matter* **15**, 3095 (2003).
- [19] I. Kibalin, A. B. Voufack, M. Souhassou, B. Gillon, J.-M. Gillet, N. Claiser, A. Gukasov, F. Porcher, and C. Lecomte, *Acta Cryst. A* **77**, 96 (2021).
- [20] P. J. Brown, *J. Phys. Chem. Solids* **65**, 1977 (2004).
- [21] A. Gukasov and P. J. Brown, *J. Phys.: Condens. Matter* **14**, 8831 (2002).
- [22] T. Chatterji, A. Stunault, and P. J. Brown, *J. Phys.: Condens. Matter* **29**, 385802 (2017).
- [23] *Entropy Measures, Maximum Entropy Principle and Emerging Applications*, edited by Karmeshu, Studies in Fuzziness and Soft Computing Vol. 119 (Springer, Berlin, 2003).
- [24] O. Magdysyuk, S. Smaalen, and R. Dinnebier, in *International Tables for Crystallography*, edited by C. J. Gilmore, J. A. Kaduk, and H. Schenk (Wiley, Hovoken, NJ, 2019), Vol. H, Chap. 4.8, pp. 473–488.
- [25] E. D. Laue, J. Skilling, and J. Staunton, *J. Magn. Reson.* (1969) **63**, 418 (1985).
- [26] E. D. Laue, M. R. Mayger, J. Skilling, and J. Staunton, *J. Magn. Reson.* (1969) **68**, 14 (1986).
- [27] See Supplemental Material at <http://link.aps.org/supplemental/10.1103/PhysRevB.105.104411> for details on notation, representation of radial functions, and MEM density reconstruction.
- [28] D. Collins, *Nature (London)* **298**, 49 (1982).
- [29] E. Ressouche, *Collection SFN* **13**, 02002 (2014).
- [30] J. S. Gardner, M. J. P. Gingras, and J. E. Greedan, *Rev. Mod. Phys.* **82**, 53 (2010).
- [31] J. G. Rau and M. J. Gingras, *Annu. Rev. Condens. Matter Phys.* **10**, 357 (2019).
- [32] I. Kibalin, A. Sazonov, and A. Goukassov, *Cryspy: CrySPy Library: PND, MEM* (Zenodo, 2020), <https://doi.org/10.5281/zenodo.4271777>.
- [33] E. Clementi and C. Roetti, *At. Data Nucl. Data Tables* **14**, 177 (1974).
- [34] G. Voronoi, *J. R. Angew. Math.* **133**, 97 (1908).
- [35] J. Boucherle, D. Givord, and J. Schweizer, *J. Phys. Colloq.* **43**, C7 (1982).
- [36] A. P. Sazonov, A. Gukasov, I. Mirebeau, and P. Bonville, *Phys. Rev. B* **85**, 214420 (2012).
- [37] A. P. Sazonov, A. Gukasov, H. B. Cao, P. Bonville, E. Ressouche, C. Decorse, and I. Mirebeau, *Phys. Rev. B* **88**, 184428 (2013).
- [38] M. Rotter, M. Le, H. Lewtas, A. Boothroyd, J. Blanco, and R. Hammerling, *J. Phys.: Conf. Ser.* **325**, 012005 (2011).
- [39] B. Z. Malkin, A. R. Zakirov, M. N. Popova, S. A. Klimin, E. P. Chukalina, E. Antic-Fidancev, P. Goldner, P. Aschehoug, and G. Dhalenne, *Phys. Rev. B* **70**, 075112 (2004).
- [40] K. Andersen, D. Argyriou, A. Jackson, J. Houston, P. Henry, P. Deen, R. Toft-Petersen, P. Beran, M. Strobl, T. Arnold, H. Wacklin-Knecht, N. Tsapatsaris, E. Oksanen, R. Woracek, W. Schweika, D. Mannix, A. Hiess, S. Kennedy, O. Kirstein, S. Petersson Årsköld *et al.*, *Nucl. Instrum. Methods Phys. Res. Sect. A* **957**, 163402 (2020).
- [41] M. Rotter and A. T. Boothroyd, *Phys. Rev. B* **79**, 140405(R) (2009).